Martínez-Botí, M. A., Foster, G. L., Chalk, T. B., Rohling, E. J., Sexton, P. F., Lunt, D. J., Pancost, R. D., Badger, M. P. S., & Schmidt, D. N. (2015). Plio-Pleistocene climate sensitivity evaluated using high-resolution CO_2 records. *Nature*, *518*(7537), 49-54. https://doi.org/10.1038/nature14145

Plio-Pleistocene climate sensitivity from a new high-resolution CO_2 record

M.A. Martinez-Boti[1,a], G.L. Foster[1,a*], T. B. Chalk[1], E.J. Rohling[2,1], P.F. Sexton[3], D.J. Lunt[4,5], R.D. Pancost[5.6], M.P.S. Badger[5,6], D.N. Schmidt[5,7]

[1]Ocean and Earth Science, University of Southampton, National Oceanography Centre Southampton, Southampton, SO14 3ZH, UK

[2]Research School of Earth Sciences, The Australian National University, Canberra 2601, Australia

[3]Centre for Earth, Planetary, Space & Astronomical Research, The Open University, Milton Keynes, MK7 6AA, UK

[4]School of Geographical Sciences, University of Bristol, University Road, Bristol, BS8 1SS, UK

[5]The Cabot Institute, University of Bristol, UK

[6]Organic Geochemistry Unit, School of Chemistry, University of Bristol, BS8 1SS, UK

[7]School of Earth Sciences, University of Bristol, Wills Memorial Building, Bristol, BS8 1RJ, UK

*corresponding author

[a] These authors contributed equally to this work.

Theory and climate modelling suggest that the sensitivity of Earth's climate to changes in radiative forcing could depend on background climate. However, palaeoclimate data have thus far been insufficient to provide a conclusive test of this prediction. Here we present new atmospheric CO_2 reconstructions based on multi-site boron-isotope records through the late Pliocene (3.3 to 2.3 Myr ago). We find that Earth's climate sensitivity to CO_2-based radiative forcing (Earth System Sensitivity) was half as strong during the warm Pliocene as during the cold late Pleistocene (0.8 to 0 Myr ago). We attribute this difference to the radiative impacts of continental ice-volume changes (ice-albedo feedback) during the late Pleistocene, because equilibrium climate sensitivity is identical for the two intervals when we account for such impacts using sea-level reconstructions.

We conclude that, on a global scale, no unexpected climate feedbacks operated during the warm Pliocene, and that predictions of equilibrium climate sensitivity (excluding long-term ice-albedo feedbacks) for our Pliocene-like future (with CO_2 levels up to maximum Pliocene levels of 450 ppm) are well described by the currently accepted range of 1.5 to 4.5 K per CO_2 doubling.

Since the start of the industrial revolution, the concentration of atmospheric CO_2 (and other greenhouse gases; GHGs) has increased dramatically (from ~280 to ~400 ppm)[1]. It has been known for over 100 years that changes in GHG concentration will cause the surface temperature of the Earth to vary[2]. A wide range of observations reveals that the sensitivity of Earth's surface temperature to radiative forcing amounts to ~3 K warming per doubling of atmospheric CO_2 concentration (with a 66% confidence range of 1.5 to 4.5 K; e.g. ref. 1,3), due to direct radiative forcing by CO_2 plus the action of a number of fast-acting positive feedback mechanisms, mainly related to atmospheric water vapour content and sea-ice and cloud albedo. Uncertainty in the magnitude of these feedbacks confounds our ability to determine the exact equilibrium climate sensitivity (ECS; the equilibrium global temperature change for a doubling of CO_2 on timescales of about a century, when all 'fast' feedbacks have had time to operate; see ref. 3 for more detail). Although the likely range of values for ECS is 1.5 to 4.5 K per CO_2 doubling, there is a small but finite possibility that climate sensitivity may exceed 5 K (e.g. ref. 1). Understanding the likely value of ECS clearly has important implications for the magnitude, eventual impact and potential mitigation of future climate change.

Any long-range forecast of global temperature (i.e. beyond the next 100 years) must also consider the possibility that ECS could depend on the background state of the climate[4,5]. That is, in a warmer world, some feedbacks that determine ECS could become more efficient and/or new feedbacks could become active to give additional warmth for a given change in radiative forcing (such as those relating to methane cycling[6], atmospheric water vapour concentrations[5,7,8], in addition to changes in the relative opacity of CO_2 to long wave radiation[5,9]). One approach to identify whether ECS depends on climate background state is to reconstruct ECS during periods in the geological past when Earth was warmer than today.

The Pliocene (2.6 to 5.3 Myr ago) is one such time, with the warmest intervals between 3.0 and 3.3 Myr ago ~3 K globally warmer than pre-industrial times[10,11], while mean sea level stood 12-32 m above the present level[12,13]. Although most of this warmth is commonly ascribed to increased atmospheric CO_2 levels[14], it has been suggested that simple comparisons of the observed temperature change in the geological record with the climate forcing from CO_2 alone are unable to constrain ECS[10]. Instead, a parameter termed Earth System Sensitivity (ESS) is defined – the change in global temperature for a doubling of CO_2 once both fast and slow feedbacks have acted and the whole Earth system has reached equilibrium (in contrast, ECS excludes the slow feedbacks; for a discussion of fast versus slow feedbacks, see ref. 3). The most important slow feedbacks are those related to ice-albedo and vegetation-albedo changes. Because of these slow feedbacks, Pliocene ESS is thought to have been ~50 % higher than ECS[10,15], with some existing geological data suggesting a Pliocene ESS range of 7-10 K per CO_2 doubling[16], which greatly exceeds a modern ESS estimate of ~4 K per CO_2 doubling[10]. If ECS was similarly enhanced, then that would imply that either extra positive fast feedbacks operated, or that existing positive fast feedbacks were more efficient, thus increasing the temperature response for a given level of CO_2 forcing.

Understanding past climate sensitivity critically depends on the accuracy of the CO_2 data used. Despite a tendency toward increased agreement between different CO_2 proxies[17], individual pCO_2 estimates for the Pliocene still range from ~190 to ~440 μatm (Fig 1a,b) and there is little coherence in the trends described by the various techniques (Fig 1a,b). This hinders any effort to accurately constrain Pliocene ECS or ESS. To better determine Pliocene CO_2 levels, we generated a new record, based on the boron isotopic composition ($\delta^{11}B$) of the surface mixed-layer dwelling planktic foraminiferal species *Globigerinoides ruber* from ODP Site 999 (Caribbean Sea, 12°44.64' N, 78°44.36' W, 2838 m water depth; Extended Data Figure 1) at more than 3× higher temporal resolution (1 sample every ~13 kyr; Fig. 1c) than previous δ^{11}B records (1 sample every 50 kyr; Fig. 1b). The δ^{11}B of *G. ruber* is a well-constrained function of pH[18] and seawater pH is well correlated with $[CO_2]_{aq}$, as both are a function of the ratio of alkalinity to total dissolved carbon in seawater. In the absence of significant changes in surface hydrography, $[CO_2]_{aq}$ is largely a function of atmospheric CO_2 levels and δ^{11}B-derived CO_2 has been demonstrated to be an accurate recorder of atmospheric CO_2 (Extended Data Figure 2a)[18-20]. Today, the surface water at Site 999 is close to equilibrium with the atmosphere with respect to CO_2 (expressed here as $\Delta pCO_2 = pCO_2^{sw}-pCO_2^{atm} = +21$ μatm; Extended Data Figure 1)[18,21] and has remained so for at least the last 130 kyr (Extended Data Figure 2)[18]. ODP Site 999 also benefits from a detailed astronomically calibrated age model[22] and high abundance of well-preserved planktic foraminifera throughout the past 4 million years[23,24]. During our study interval it is also unlikely to have been influenced by long-term oceanographic changes such as the emergence of the Panama Isthmus ~3.5 Myr ago (see detailed discussion in ref. 23). To increase confidence that atmospheric CO_2 changes are driving our pH (and hence our pCO_2^{sw}) record for ODP Site 999 and that the air:sea CO_2 disequilibrium remained similar to modern values, we also present lower-resolution δ^{11}B data from *G. ruber* from ODP Site 662 (equatorial Atlantic, Fig. 1c; 1°23.41'S, 11°44.35°W, 3821 m water depth; Extended Data Figure 1), where current mean annual ΔpCO_2 is +29 μatm with a seasonal maximum of +41 μatm[21]. Analytical methodology and information detailing precisely how pCO_2^{sw} is calculated, with full propagation of uncertainties, can be found in the Methods section (with full δ^{11}B and pCO_2 in Supplementary Information Tables 1&2).

A new record of Pliocene pCO_2 change

Where our data for both sites overlap in time, reconstructed pCO_2^{atm} values between 2.3 and 3.3 Myr ago agree within uncertainty (Fig 1d; Extended Data Figure 3), and are consistent with most independent records (see Fig 1a,b; Extended Data Figure 2b,c), confirming that the variations we observe are predominantly driven by changes in atmospheric CO_2 concentrations. However, the enhanced resolution of our δ^{11}B-pCO_2^{atm} record (Fig. 1d) also reveals a hitherto undocumented[16,23,25,26] level of structure in the CO_2 variability during the 1 million year period investigated, including a transition centred on 2.8 Ma, spanning ~200 kyr, where average pCO_2^{atm} undergoes a decrease of ~65 μatm (Fig 1d).

Detailed atmospheric CO_2 measurements from ice cores show orbital-scale (~100 kyr) oscillations in pCO_2^{atm} with a peak-to-trough variation of ~80-100 μatm through the late Pleistocene (90 % of the pCO_2 values lie between +36 and –41 μatm of the long-term mean; Extended Data Figures 2, 4)[27-29]. Once the long-term trend is removed from our Plio-Pleistocene data (thick blue line in Fig 1d), and we have taken into account our larger analytical uncertainty (see Methods), we observe orbital-scale variations in our δ^{11}B-pCO_2^{atm} record of only slightly smaller amplitude than the ice-core pCO_2^{atm} record (0-0.8 Myrs) and for the last 2 Myrs in other δ^{11}B-based records[19,20,30] (Extended Data Figure 4 and Methods), which is in clear contrast with the benthic δ^{18}O which shows increasing variability over the last 3 Myrs (Fig 1e and Extended Data Figure 4).

Given the different amplitudes of climate variability, the observed similarity between Pliocene and late Pleistocene pCO_2^{atm} variability seems counter-intuitive given the notion that CO_2 is a key factor in amplifying glacial-interglacial climate change[27-29,31,32]. This is illustrated by a well-defined non-linear relationship in a cross plot between deep-sea benthic δ^{18}O and $\ln(CO_2/C_o)$ (where C_o = pre-industrial CO_2 = 278 μatm), which accounts for the logarithmic nature of the climate forcing by CO_2 (Fig. 2b). Note also the clear overlap between Pleistocene (0-2.2 Myrs) ice-core CO_2 measurements and δ^{11}B-based CO_2 reconstructions in this plot (Fig. 2b; Extended Data Figure 2). A similar relationship is also evident in raw δ^{11}B-space (Fig. 2a). Below an inflection at about 275±15 μatm pCO_2^{atm} (equating to $\ln(CO_2/C_o) \approx 0$) benthic δ^{18}O shows a steeper relationship with CO_2-based forcing than it does above this value (Fig. 2). This likely reflects some combination of: (i) growth of larger northern hemisphere ice sheets at pCO_2^{atm} below 275±15 μatm[33] increasing radiative ice-albedo feedback and amplifying climate forcing by CO_2 change; (ii) an increase in oxygen isotope fractionation in precipitation with increasing size of the ice sheets, which leads to a proportionally greater ^{18}O enrichment in seawater[34]; and (iii) potentially stronger deep-sea cooling at low pCO_2^{atm} due to the high-latitude-focussed influences of the ice-albedo feedback process. These findings highlight the profound impacts of northern hemisphere ice-sheet growth on climate variability in the Pleistocene [31,32], relative to the Pliocene (Fig. 2b).

Our new data show that the ~275±15 μatm threshold was first crossed at ~2.8 Ma during Marine Isotope Stage (MIS) G10 (Fig. 1d, horizontal dashed line), and – more persistently – during subsequent Marine Isotope Stages G6 (2.72 Myr ago), G2 (2.65 Myr ago), and 100 (2.52 Myr ago), when values as low as 233^{+63}_{-53} μatm (95% confidence) were reached and when intervening interglacial values also seem to have been suppressed (Fig. 1c,d). These isotope stages are significant in that they are associated with an increase in the amplitude of glacial-interglacial sea-level oscillations (Extended Data Figure 5b)[12,13,35] and coincide with the timing of the first substantial continental glaciations of Europe, North America and the Canadian Cordillera, as reconstructed by Ice-rafted debris and observations of relic continental glacial deposits[36-38]. Hence, our new high-resolution pCO_2^{atm} record robustly confirms previous hypotheses[16,23,25,39] (based on low-resolution CO_2 data) that the first substantial stages of glaciation on the northern hemisphere, as well as a recently recognised deep-sea cooling during the late Pliocene/early Pleistocene[13], coincided with a significant decline in mean atmospheric pCO_2^{atm} at 2.7-2.9 Ma of ~40-90 μatm ($\text{mean}_{3.0\text{-}3.2\text{Ma}} - \text{mean}_{2.4\text{-}2.7\text{Ma}}$ = 66 ± 26 μatm; p <0.001 (two-tailed), n=40).

Efficiency of climate feedbacks

The high fidelity of the boron isotope pH/pCO_2^{atm} proxy (Extended Data Figure 2), coupled with the high resolution of our new pCO_2^{atm} record, offers an opportunity to examine the sensitivity of Earth's climate system to forcing by CO_2 during a period when Earth's climate was, on average, warmer than today[40]. For this exercise, global temperature estimates are also needed. We consider two approaches for this. The first is an estimate of global mean annual surface air temperature change (ΔMAT) over the last 3.5 million years, from a scaling of the northern hemisphere climate required to drive an ice-sheet model to produce deep ocean temperature and ice-volume changes consistent with benthic δ^{18}O data (Fig 3a,b)[35]. This approach produces a continuous record of global temperature that agrees well with independent constraints for discrete time intervals (see ref. 35).

We supplement ΔMAT with a record from a second approach, which is independent from benthic δ^{18}O values. For this, we generated a sea surface temperature stack (SSTst) from 0 to 3.5 Myr ago (Fig. 3c,d), comprising 10 high-resolution (average ~4 kyr) SST records based on $U^{K'}_{37}$ alkenone unsaturation ratios, from latitudes between 41 °S and 57 °N. The selected sites (see Extended Data Figure 1b) all offer near-continuous temporal coverage of the last 3.5 Myr (see Methods). Our SSTst record agrees well with independent, higher density compilations of global SST change[32,41] (Fig 3c blue line), indicating that SSTst offers a reliable approximation of global SST change (see Methods for more details). Moreover, our SSTst allows us to directly compare the major SST changes, within the same archives, between the Plio-Pleistocene and late Pleistocene.

When comparing temperature records from the two approaches considered, it must be emphasized that ΔMAT reflects global mean annual surface air temperature change, while SSTst approximates global mean sea surface temperature change. Hence, their amplitudes of variability will be different, mainly because SSTst does not include temperature changes over land. Approximately, $\Delta SST = \Delta MAT * 0.66$ (ref. 32,42), but direct conversion is not needed here, as we merely aim to contrast Pliocene climate behaviour with that for the Pleistocene, within the same data types.

To determine the sensitivity of global SST and ΔMAT to CO_2 forcing in the Pliocene and Pleistocene, we use time series of forcing calculated from our new and existing CO_2 records (Fig 3e to h), and regress these against both ΔMAT and SSTst (Fig 3a to d; Supplementary Information Tables 1-3). The regression slopes then describe the average temperature change (ΔT in K) per W per m^2 of forcing

(ΔF) for each time interval. These gradients therefore approximate the commonly used sensitivity parameter ($S = \Delta T/\Delta F$ K W^{-1} m^2) for describing global temperature change for a given forcing[3]. In this scheme, a doubling of atmospheric CO_2 is equivalent to a forcing of 3.7 W m^{-2}, so that for the 66% confidence interval of modern climate sensitivity quoted by ref. 1, the present-day equilibrium value of S (S^a, after ref. 3) is 1.5/3.7 to 4.5/3.7 = 0.4 to 1.2 K W^{-1} m^2. However, using palaeoclimate data it is not possible to determine the direct equivalent of S^a; instead, such studies constrain a 'past' parameter (S^p), which includes the combined action of both fast and slow feedbacks[3]. Note that Earth System Sensitivity, ESS (in K) = S^p x 3.7. Explicit accounting for slow feedback processes in determinations of S^p can make it approximate S^a (ref. 3). Following ref. 3, an S^p estimate after accounting for carbon-cycle feedback is indicated by S_{CO2}, and one accounting for both carbon-cycle and land-ice-albedo feedbacks is $S_{CO2,LI}$, where the latter gives a useful approximation of S^a. We follow this approach, using $S^p = \Delta MAT/\Delta F$ and $S^{p,SST} = \Delta SST/\Delta F$, both in K W^{-1} m^2. Note that our determinations of the sensitivity parameter are based on our entire reconstructed time series, rather than on a simple comparison between a limited Pliocene average and the modern average, as was done in previous studies[3,16]. Since we calculate a S^p (and $S^{p,SST}$) for the Pliocene and compare this to the late Pleistocene S^p (and $S^{p,SST}$), we also avoid complications due to independent changes in boundary conditions (such as topographic changes)[39] because we assess sensitivity within each relatively short time window (2.3 to 3.3 Ma vs. 0 to 0.8 Ma). In addition, our approach emphasizes relative changes in CO_2 levels and temperature over the intervals considered, rather than absolute values. This improves accuracy because relative changes are much better constrained than absolute temperature and pCO_2^{atm} values from proxy data (see Methods for further discussion).

Preliminary regression of ΔMAT against Pliocene pCO_2^{atm} identified one data point (at 2362 kyr; white circle in Fig. 1d & 2) with a particularly large residual and significant leverage on the least squares regression (a high Cook's distance). With interglacial-like pCO_2^{atm} values but glacial-like $\delta^{18}O$ values (Fig 2), this point may reflect a chronological error, or a short period of unusually high air:sea disequilibrium with respect to CO_2 at ODP Site 999. To avoid the influence of this one point on subsequent linear regressions, we have removed it from our δ^{11}B-pCO_2^{atm} record. The remaining pCO_2^{atm} data (73 points) were interpolated to a constant resolution (1 kyr), smoothed with a 20 kyr moving average to reduce short-term noise and resampled back to the original data spacing (~1 sample every 13 kyr). A Monte Carlo approach was followed to determine uncertainties for this smoothed record given the uncertainty in the δ^{11}B-derived pCO_2^{atm}. Radiative forcing changes due to pCO_2^{atm} changes are calculated using $\Delta F_{CO2} = 5.35*\ln(CO_2/C_o)$ W m^{-2}; where $C_o = 278$ μatm (Fig 3)[43]. We ignore mean annual forcing by orbital variations because it is small (<0.5 W m^{-2} with a periodicity of 100 to 400 kyr)[31,32] and averages out over the length of our records. Linear regressions of ΔMAT and SSTst *versus* ΔF_{CO2} were performed using an approach that yields a probabilistic estimate of slope, and hence sensitivity to CO_2 forcing ($S_{CO2} = \Delta T/\Delta F_{CO2}$ or $S_{CO2,LI} = \Delta T/\Delta F_{CO2,LI}$), which fully accounts for uncertainties in both X and Y variables (see Methods; Fig 4). Fig 5a-d displays probability distribution functions (pdfs) of the determinations of slope for each time interval. This analysis reveals that, irrespective of the global temperature record used (ΔMAT or SSTst), the average global sensitivity of Earth's climate to forcing by CO_2 only (S_{CO2}) is approximately 2x higher for the Pleistocene than it is for the Pliocene (Fig 4&5). This validates previous inferences of a strong additional feedback factor during the Pleistocene (at pCO_2^{atm} levels below ~280 μatm), which likely arises from the growth and retreat of large northern hemisphere ice sheets and their role in changing global albedo[31,32].

Given that, to a first order, the Earth system responds to radiative forcing in a consistent fashion, largely independent of the nature of that forcing[8], we can determine the climate forcing arising from continental ice albedo changes via a relatively simple parameterisation of sea-level change (ΔF_{LI} = sea-level change (m) × 0.0308 W m^{-2}; following ref. 31,32). Several reconstructions of sea-level change partially or completely span the last 3.5 Ma (e.g., ref. 13, 35, 44, 45, and 46 recalculated by 12), and we explore the implications of each of these independent records. Cross-plots of combined

CO_2 and ice-albedo forcing ($\Delta F_{CO2} + \Delta F_{LI} = \Delta F_{CO2,LI}$) *versus* ΔMAT and ΔSSTst are shown in Fig 4 for the Pliocene and Pleistocene. Fig 5e-h displays the influence of choices of temperature and sea-level record on our determinations of $S_{CO2,LI}$ (= $\Delta T/\Delta F_{CO2,LI}$). In contrast to S_{CO2}, $S_{CO2,LI}$ is similar for both the Pliocene and Pleistocene, regardless of temperature record or other parameter choices (Fig 5). This robustly indicates that the apparent difference between Pliocene and Pleistocene climate sensitivity arises almost entirely from ice-albedo feedback influences. It also implies that all of the other feedbacks that amplify climate forcing by CO_2 (e.g. sea-ice and cloud albedo, water vapour, vegetation, aerosols, other GHGs) must have operated with rather similar efficiencies during both the Pliocene and Pleistocene. Thus, we find no evidence that additional (unexpected) positive feedbacks had become active to amplify Earth system sensitivity to CO_2 forcing during the warm Pliocene. Alternatively, if additional positive feedbacks did become active (e.g. increase in steady-state methane concentration or changes in cloud properties), then their effect must have been negated by the loss of other amplifying feedbacks (e.g. Arctic sea-ice) or the addition of more negative feedbacks. This finding is at odds with previous studies (e.g. ref. 16,47) most likely because of differences in our approach to determine Pliocene climate sensitivity (i.e. we determine a *within*-Pliocene sensitivity) and shortcomings in the proxy systems used by the earlier investigations, both in terms of CO_2 and temperatures (e.g. see ref. 48). For instance, Fig 1d (and Extended Data Figure 2) indicate that both orbital-scale variability in pCO_2^{atm} and the major decline at 2.7-2.9 Ma are absent from the previously used[16] alkenone-based pCO_2^{atm} records and as a result regressions of temperature and alkenone-derived forcing are poorly defined (Extended Data Figure 2d-f).

Constraints on Climate Sensitivity

Using the geological record to directly estimate ECS (and thus S^{a}) is problematic because information on the appropriate magnitude of a number of key feedbacks (such as vegetation-albedo) is typically unavailable[3]. Nonetheless, considerable effort has determined that ECS estimates based on the last glacial maximum fall within the range of ECS estimates from other approaches (1.5 to 4.5 K per CO_2 doubling, or 0.4 to 1.2 K W^{-1} m^2; ref. 1). Our analysis implies that a similar ECS applies to the Pliocene and early Pleistocene (2.3 to 3.3 Ma; Fig 5; Supplementary Information Table 4). In addition, our estimate of Pliocene S_{CO2} using ΔMAT lies within a range of 0.6 to 1.5 K W^{-1} m^2 (at 95% confidence), meaning that, once all feedbacks have played out for future CO_2 doubling, ESS (= S_{CO2} x 3.7) will very likely (95% confidence) be <5.2 K and will likely (68% confidence) fall within a range of 3.0 to 4.4 K (Supplementary Information Table 4).

In May 2013, atmospheric CO_2 levels crossed the 400 ppm threshold to values last seen during the Pliocene (Fig. 1c). Given current CO_2 emission rates, global temperatures may reach those typical of the warm periods of the Pliocene by 2050[1]. Our findings suggest that, if the Earth system behaves in a similar fashion to how it did during the Pliocene as it continues to warm in the coming years, an ECS of 1.5 to 4.5 K per CO_2 doubling[1] likely provides a reliable description of the Earth's temperature response to climate forcing, at least for global temperature rise up to 3 K above the pre-industrial level. Studies of even warmer intervals in the deeper geological past (well before 3.3 Myr ago) are needed to determine whether any additional climate feedbacks should be expected as the Earth warms even further into the 22nd Century if CO_2 emissions continue unabated.

References

1 IPCC, 2013: Climate Change 2013: The Physical Science Basis. Contribution of Working Group I to the Fifth Assessment Report of the Intergovernmental Panel on Climate Change [Stocker, T.F., D. Qin, G.-K. Plattner, M. Tignor, S.K. Allen, J. Boschung, A. Nauels, Y. Xia, V. Bex and P.M. Midgley (eds.)]. Cambridge University Press, Cambridge, United Kingdom and New York, NY, USA, 1535 pp (2013).

2 Arrhenius, S. On the influence of carbonic acid in the air upon the temperature of the ground. *Philosphical Magazine and Journal of Science* 5, 237-276 (1896).

3 Rohling, E. J. *et al.* Making sense of palaeoclimate sensitivity. *Nature* **491**, 683-691, doi:10.1038/nature11574 (2012).

4 Crucifix, M. Does the Last Glacial Maximum constrain climate sensitivity? *Geophys. Res. Lett.* 33, doi:10.1029/2006GL027137, 022006 (2006).

5 Caballero, R. & Huber, M. State-dependent climate sensitivity in past warm climates and its implication for future climate projections. *PNAS,* 110 (35), 14162-14167doi:www.pnas.org/cgi/doi/10.1073/pnas.1303365110 (2013).

6 Beerling, D. J., Fox, A., Stevenson, D. S. & Valdes, P. J. Enhanced chemistry-climate feedbacks in past greenhouse worlds. *PNAS* 108, 9770-9775, doi: 10.1073/pnas.1102409108 (2011).

7 Meraner, K., Mauritsen, T. & Voigt, A. Robust increase in equilibrium climate sensitivity under global warming. Geophys. Res. Lett. 40, 5944-5948, doi:10.1002/2013GL058118 (2013).

8 Hansen, J. et al. Efficacy of climate forcings. *J. Geophys. Res*. 110, doi:10.1029/2005JD005776 (2005).

9 Byrne, B. & Goldblatt, C. Radiative forcing at high concentrations of well-mixed greenhouse gases. *Geophys. Res. Lett.*41, 152-160, doi:10.1002/2013GL058456. (2013).

10 Lunt, D. J. et al. Earth system sensitivity inferred from Pliocene modelling and data. *Nature Geoscience* 3, 60-64, doi:10.1038/NGEO706 (2010).

11 Haywood, A. M. & Valdes, P. J. Modelling Pliocene warmth: contribution of atmosphere, oceans and cryosphere. *Earth Planet. Sci. Lett.* 218, 363-377 (2004).

12 Miller, K. G. et al. High tide of the warm Pliocene: Implications of global sea level for Antarctic deglaciation. *Geology* 40, 407-410, doi:10.1130/G32869.1 (2012).

13 Rohling, E. J. et al. Sea-level and deep-sea-temperature variability over the past 5.3 million years. *Nature* 508, 477-482, doi:10.1038/nature13230 (2014).

14 Lunt, D. J. et al. On the causes of mid-Pliocene warmth and polar amplification. Earth Planet. Sci. Lett. 321-322, 128-138, doi:10.1016/j.epsl.2011.12.042 (2012).

15 Haywood, A. M. et al. Large-scale features of Pliocene climate: results from the Pliocene Model Intercomparison Project. *Clim. Past* 9, 191-209, doi:10.5194/cp-9-191-2013 (2013).

16 Pagani, M., Liu, Z., LaRiviere, J. & Ravelo, A. C. High Earth-system climate sensitivity determined from Pliocene carbon dioxide concentrations. *Nature Geoscience* 3, 27-30, doi:DOI: 10.1038/NGEO724 (2010).

17 Beerling, D. J. & Royer, D. L. Convergent Cenozoic CO_2 history. *Nature Geoscience* 4, 418-420, doi:10.1038/ngeo1186 (2011).

18 Henehan, M. J. et al. Calibration of the boron isotope proxy in the planktonic foraminifera *Globigerinoides ruber* for use in palaeo-CO_2 reconstruction. *Earth Planet. Sci. Lett.* 364, 111-122, doi:10.1016/j.epsl.2012.12.029 (2013).

19 Hönisch, B. & Hemming, N. G. Surface ocean pH response to variations in pCO_2 through two full glacial cycles. *Earth Planet. Sci. Lett.* 236, 305-314 (2005).

20 Foster, G. L. Seawater pH, pCO2 and $[CO_3^{2-}]$ variations in the Caribbean Sea over the last 130 kyr: A boron isotope and B/Ca study of planktic foraminifera. *Earth Planet. Sci. Lett.* 271, 254-266 (2008).

21 Takahashi, K. et al. Climatological mean and decadal change in surface ocean pCO_2, and net sea-air CO_2 flux over the global oceans. *Deep-Sea Res. II* 56, 554-577 (2009).

22 Lisiecki, L. E. & Raymo, M. E. A Pliocene-Pleistocene stack of 57 globally distributed benthic $\delta^{18}O$ records. *Paleoceanography* 20, doi: 10.1029/2004PA001071 (2005).

23 Bartoli, G., Hönisch, B. & Zeebe, R. Atmospheric CO_2 decline during the Pliocene intensification of Northern Hemisphere Glaciations. *Paleoceanography* 26, PA4213, doi:4210.1029/2010PA002055 (2012).

24 Davis, C.V., Badger, M.P.S., Bown, P.R. & Schmidt, D.N. The response of calcifying plankton to climate change in the Pliocene, *Biogeosciences*, 10, 6131-6139 (2013).

25 Seki, O. et al. Alkenone and boron based Plio-Pleistocene pCO_2 records. *Earth Planet. Sci. Lett.* 292, 201-211 (2010).

26 Badger, M. P. S., Schmidt, D. N., Mackensen, A. & Pancost, R. D. High resolution alkenone palaeobarometry indicates relatively stable pCO_2 during the Pliocene (3.3 to 2.8 Ma). *Philos. Trans. Royal Soc. A* 347, 20130094, doi: 10.1098/rsta.2013.0094 (2013).

27 Petit, J. R. et al. Climate and atmospheric history of the past 420,000 years from the Vostok ice core, Antarctica. *Nature* 399, 429-436 (1999).

28 Lüthi, D. et al. High-resolution carbon dioxide concentration record 650,000-800,000 years before present. *Nature* 453, 379-382, doi:10.1038/nature06949 (2008).

29 Siegenthaler, U. et al. Stable carbon cycle-climate relationship during the Late Pleistocene. *Science* 310, 1313-1317 (2005).

30 Hönisch, B., Hemming, G., Archer, D., Siddal, M. & McManus, J. Atmospheric carbon dioxide concentration across the Mid-Pleistocene Transition. *Science* 324, 1551-1554 (2009).

31 Köhler, P. et al. What caused Earth's temperature variations during the last 800,000 years? Data-based evidence on radiative forcing and constraints on climate sensitivity. *Quat. Sci. Reviews* 29, 129-145, doi:10.1016/j.quascirev.2009.09.026 (2010).

32 Rohling, E. J., Medina-Elizalde, M., Shepherd, J. G., Siddall, M. & Stanford, J. D. Sea surface and High-lattitude temperature sensitivity to radiative forcing of climate over several glacial cycles. *J. Climate* 25, 1635-1656, doi:10.1175/2011JCLI4078.1 (2012).

33 DeConto, R. M. et al. Thresholds for Cenozoic bipolar glaciation. *Nature* 455, 652-656 (2008).

34 Shackleton, N. Oxygen isotope analyses and Pleistocene temperatures re-assessed. *Nature* 215, 15-17 (1967).

35 van de Wal, R. S. W., de Boer, B., Lourens, L. J., Köhler, P. & Bintanja, R. Reconstruction of a continuous high-resolution CO_2 record over the past 20 million years *Clim. Past* 7, 1459-1469, doi:10.5194/cp-7-1459-2011 (2011).

36 Balco, G. & Rovey, C. W., II. Absolute chronology for major Pleistocene advances of the Laurentide Ice Sheet. *Geology* 38, 795-798, doi:10.1130/G30946.1 (2010).

37 Bailey, I. et al. An alternative suggestion for the Pliocene onset of major northern hemisphere glaciation based on geochemical provenance of North Atlantic Ocean ice-rafted debris. *Quat. Sci. Reviews* 75, 181-194, doi:10.1016/j.quascirev.2013.06.004 (2013).

38 Hidy, A. J., Gosse, J. C., Froese, D. G., Bond, J. D. & Rood, D. H. A latest Pliocene age for the earliest and most extensive Cordilleran Ice Sheet in northwestern Canada. *Quat. Sci. Reviews* 61, 77-84, doi:10.1016/j.quascirev.2012.11.009 (2013).

39 Lunt, D. J., Foster, G. L., Haywood, A. M. & Stone, E. J. Late Pliocene Greenland glaciation controlled by a decline in atmospheric CO2 levels. *Nature* 454, 1102-1105 (2008).

40 Dowsett, H. J. et al. Assessing confidence in Pliocene sea surface temperatures to evaluate predictive models. *Nature Climate Change* 2, 365-371, doi:10.1038/NCLIMATE1455 (2012).

41 Shakun, J. D. et al. Global warming preceded by increasing carbon dioxide concentrations during the last deglaciation. *Nature* 484, 49-54, doi:10.1038/nature10915 (2012).

42 Williams, R. G., Goodwin, P., Ridgwell, A. & Woodworth, P. L. How warming and steric sea level rise relate to cumulative carbon emissions. *Geophys. Res. Lett.* 39, doi: 10.1029/2012GL052771 (2012).

43 Myhre, G., Highwood, E. J., Shine, K. P. & Stordal, F. New estimates of radiative forcing due to well mixed greenhouse gases. *Geophys. Res. Lett.* 25, 2715-2718 (1998).

44 Rohling, E. J. et al. Antarctic temperature and global sea level closely coupled over the past five glacial cycles. *Nature Geoscience* 2, 500-504, doi:10.1038/ngeo557 (2009).

45 Elderfield, H. et al. Evolution of ocean tempeature and ice volume through the Mid-Pleistocene climate transition. *Science* 337, 704-709, doi:10.1126/science.1221294 (2012).

46 Naish, T. R. & Wilson, G. S. Constraints on the amplitude of Mid-Pliocene (3.6-2.4 Ma) eustatic sea-level fluctuations from the New Zealand shallow-marine sediment record. *Philos. Trans. Royal Soc. A* 367, 169-187, doi: 10.1098/rsta.2008.0223 (2009).

47 Federov, A. V. et al. Patterns and mechanisms of early Pliocene warmth. *Nature* 496, 43-49, doi:10.1038/nature12003 (2013).

48 O'Brien, C.L. et al., 2014. High sea surface temperatures in tropical warm pools during the Pliocene. *Nature Geoscience* 7, 606-611, doi: 10.1038/ngeo2194.

49 Zhang, Y. G., Pagani, M., Liu, Z., Bohaty, S. M. & DeConto, R. M. A 40-million-year history of atmospheric CO_2. *Philos. Trans. Royal Soc. A* 371, 20130096 (2013).

50 Kürschner, W. M., van der Burgh, J., Visscher, H. & Dilcher, D. L. Oak leaves as biosensors of late Neogene and early Pleistocene paleoatmospheric CO_2 concentrations. *Mar. Micropal*. 27, 299-312 (1996).

Supplementary Information is linked to the online version of the paper at www.nature.com/nature

Acknowledgements This study used samples provided by the International Ocean Discovery Program (IODP). We thank Andy Milton at the University of Southampton for maintaining the mass spectrometers used in this study. Soraya Cherry and Thorsten Garlichs are acknowledged for their help with sample preparation and Diederik Liebrand is thanked for his assistance with time series analysis. This study was funded by NERC grants NE/H006273/1 to RDP, GLF, DJL and DNS (which supported MAMB and MPSB) and NE/I006346/1 to PFS and GLF. MAMB was also supported by the European Community through a Marie Curie Fellowship and EJR was supported by 2012 Australian Laureate Fellowship FL120100050. GLF also wishes to acknowledge the support of Yale University (as Visiting Flint Lecturer).

Author Contributions MAMB and TBC collected the data and all relevant calculations were performed by GLF. GLF, MAMB and TBC constructed the first draft of the manuscript and all authors contributed specialist insights that helped refine the manuscript. PFS aided sample preparation for δ^{11}B analysis and refined the age models used for ODP Sites 999 and ODP 662 and GLF, RDP, DJL and DNS conceived the study. MAMB and GLF contributed equally to this work.

Author Information Reprints and permissions information is available at www.nature.com/reprints. The authors declare no competing financial interests. Readers are welcome to comment on the online version of the paper. Correspondence and requests for materials should be addressed to GLF (gavin.foster@noc.soton.ac.uk).

Figure Legends

Figure 1. Records of late Pliocene/early Pleistocene pCO_2^{atm}. (a) pCO_2^{atm} based on $\delta^{13}C$ of sedimentary alkenones (dark green circles (ODP 999)[25]; aquamarine squares (ODP 999)[26]; dark orange (ODP 1208)[16], purple circles (ODP 806)[16]; dark red squares (ODP 925)[49]). Error bars are uncertainty in pCO_2^{atm} at the 95% level of confidence. (b) $\delta^{11}B$ of planktic foraminifera from ODP 999 (blue closed circles for *G. sacculifer* and squares[25] for *G. ruber*[25]; red squares for *G. sacculifer*[23]) and stomatal density of fossil leaves (purple filled circle)[50]. Error bars are uncertainty in pCO_2^{atm} at the 95% level of confidence. (c) New boron isotope data from ODP 999 (blue circles) and ODP 662 (red circles). Error bands for ODP 999 denote 1sd (dark blue) and 2sd (light blue) analytical uncertainty, error bars for ODP 662 show 2sd analytical uncertainty. (d) Atmospheric pCO_2 (μatm) determined from data shown in (c) for ODP 999 (blue circles) and ODP 662 (red circles). Error band encompasses 68% (dark blue) and 95% (light blue) of 10,000 Monte Carlo simulations of pCO_2^{atm} using the data in (c) and a full propagation of all the key uncertainties (see Methods). For ODP 662 error bars encompass 95% of 10,000 simulations. Dotted lines show the modelled threshold of northern hemisphere glaciation (280 μatm)[33]. (e) Benthic $\delta^{18}O$ stack[22], prominent marine isotope stages are labelled (blue for glacial, red for interglacial stages). Thick lines on several panels are non-parametric smoothers through the data. Blue open circle on (d) highlights the data point that is identified as outlier in Fig 2 and not used in subsequent regressions.

Figure 2. Relationship between $\delta^{11}B$, climate forcing from CO_2 and $\delta^{18}O$. (a) $\delta^{11}B$ vs. $\delta^{18}O$ and (b) $\ln(CO_2/C_o)$ vs. $\delta^{18}O$ for data from the last 3 million years. $\ln(CO_2/C_o)$ is defined in the text. Boron data in (a) are from this (blue open and closed circles) and published studies (green circles[30]; blue

triangles[20]). Ice-core CO_2 data shown as open red circles[27-29]. The vertical dashed line is at a CO_2 of 278 μatm. The data point removed from subsequent regression analysis is highlighted as open blue circles. Note that the δ^{11}B-pCO_2 data from ref. 23 are not plotted for clarity. The black line is a non-parametric regression through all the data shown. The δ^{11}B data from ref. 30 have been corrected for laboratory and inter-species differences through a comparison between core-top δ^{11}B values.

Figure 3. Pleistocene and late Pliocene time series. (a) and (b) mean annual surface air temperature change (ΔMAT)[35], (c) and (d) sea surface temperature change (ΔSST; this study in red and from a stack of a more comprehensive compilation[32] in blue). Uncertainty envelopes at 95% confidence for both temperature records are shown in red. (e) ΔF_{CO2} for the Pleistocene from ice-core data[27-29]. (f) ΔF_{CO2} for the late Pliocene calculated using the CO_2 data from this study. (g) $\Delta F_{CO2,LI}$ calculated using data in (e) and published sea-level records (R14[13], VDW11[35] and from ref. 44 for 0-520 kyr and ref. 45 for 520 to 800 kyr, R09+E12). (h) $\Delta F_{CO2,LI}$ for the late Pliocene calculated using the CO_2 data from this study and published sea-level records (ref. 46 recalculated by ref. 12, N09, R14[13], VDW11[35]). Error bands in (e) to (h) represent the uncertainty in smoothed CO_2 record and sea-level (68% and 95% confidence in light and dark respectively) propagated using a Monte Carlo approach (n=1000) for each reconstruction.

Figure 4. Cross plots of forcing and temperature response. (a) ΔMAT vs. ΔF_{CO2} and (b) to (d) ΔMAT vs. $\Delta F_{CO2,LI}$ for the following sea-level records detailed in the caption for Figure 3: (b) R09+E12[44,45] and N09[12,46] (c) VDW11[35], (d) R14[13]. (e) ΔSST vs. ΔF_{CO2} and (f) to (h) ΔSST vs. $\Delta F_{CO2,LI}$ for the same sea-level records as in panels (b) to (d). In all panels late Pleistocene data (0-800 kyr) are shown as red open circles and late Plio-Pleistocene (2300-3300 kyr) as blue open circles. Regression lines fitted by least-squares regression are also shown in the appropriate colour (shaded bands represent 95% confidence intervals). For (a) to (d) the temperature record is that of ref. 35 and for (e) to (h) it is SSTst from this study. In all cases the slope (m) and standard error uncertainty are determined by least squares regression. Also shown are the *p* values for the regressions.

Figure 5. **Probability density functions of the slope from regressions of temperature against climate forcing.** (a,c,e,g) ΔMAT and (b,d,f,h) ΔSST against ΔF_{CO2} and $\Delta F_{CO2,LI}$ for the Pleistocene (a, b, e, f) and Pliocene (c, d, g, h), taking into account the uncertainties on all variables (see text). In (e) to (h) individual pdfs are shown for different choices of sea-level, the combined pdf shown in bold is the sum of these different pdfs and therefore also incorporates uncertainty related to the choice of sea-level record. Also shown and labelled are the median (bold), 68th percentile (dot-dash) and 95th percentiles (dotted).

Methods

Sample locations. We present new data from two deep ocean sites: ODP Site 999 (Caribbean Sea, 12°44.64'N and 78°44.36'W) and ODP Site 662 (Equatorial Atlantic, 1°23.41'S, 11°44.35'W). Both sites have well-constrained age models for the Pliocene and are part of the Lisiecki and Raymo benthic foraminifera $\delta^{18}O$ stack[22] (hereafter LR04). Sedimentation rates are comparable between the sites (~3 cm/kyr at ODP 999 and ~4 cm/kyr at ODP 662). At ODP Site 999, seventy four samples were analysed at an average temporal resolution of around 1 sample every 13 kyr, targeting several glacial and interglacial maxima. ODP Site 662 was analysed at much lower resolution (8 samples in 1000 kyr = 1 sample every 125 kyr on average), and the chosen samples were limited to peak interglacial conditions to avoid potential upwelling influences during glacial periods[51]. The extent of the modern air-sea CO_2 disequilibrium at each location is displayed in Extended Data Fig 1a.

Analytical methodology. Between 90 and 200 individuals of *Globigerinoides ruber* (~10 µg/shell) were picked from the 300-355 µm size fraction from ODP Sites 999 and 662. Foraminiferal samples were crushed between cleaned glass microscope slides and subsequently cleaned according to established oxidative cleaning methods[52-54]. After cleaning, samples were dissolved in ~0.15 M Teflon-distilled HNO_3, centrifuged and transferred to 5 ml Teflon vials for storage. An aliquot (~20 µl;

~7% of the total sample) was taken for trace element analysis. Boron was separated from the dissolved samples using Amberlite IRA-743 boron-specific anion exchange resin following established procedures[20]. Boron isotope ratios were measured on a Thermo Scientific Neptune multicollector inductively coupled plasma mass spectrometer (MC-ICPMS) at the University of Southampton according to methods described elsewhere[18,20,54].

External reproducibility of $\delta^{11}B$ analyses is calculated following the approach of ref. 54, and is described by the relationship:

$$2\sigma = 1.87 \cdot \exp^{-20.6[^{11}\mathrm{B}]} + 0.22 \cdot \exp^{-0.43[^{11}\mathrm{B}]} \qquad [1]$$

where $[^{11}B]$ is the intensity of the ^{11}B signal in volts (see ref. 18 for further details).

Trace elements were measured on a Thermo Scientific Element 2 single collector ICPMS at the University of Southampton, following established methods[20]. Over the period 2012-2013, analytical reproducibility for Mg/Ca was ± 2.7% (2σ). Raw Mg/Ca ratios were corrected for changes in the Mg/Ca ratio of seawater (Mg/Ca_{sw}) using the approach of ref. 55 using the power-law modification of ref. 56 and the modelled Mg/Ca_{sw} of ref. 57. Specifically, we use a H value[56] of 0.41, originally derived for *Globigerinoides sacculifer*[58], as no species-specific H value is currently available for *G. ruber* (for extended discussion, see ref. 48). The following equation[56,59] was therefore used to derive calcification temperatures from our Mg/Ca ratios, which also includes a depth correction to account for the influence of dissolution on shell Mg/Ca ratios.

$$T(\,^{o}C) = \frac{\ln\left(\left(\frac{Mg}{Ca_{test}}\right) / \left(E \times \left(\left(\frac{Mg}{Ca}\right)_{sw}^{t}\right)^{H}\right)\right)}{0.09} + (0.61 \times Z) \qquad [2]$$

Where $\left(\frac{Mg}{Ca}\right)_{sw}^{t}$ is the Mg/Ca ratio of seawater at the time of interest, Z is the core depth in km and E is defined by the following equation[56]:

$$E = \frac{0.38}{\left(\left(\frac{Mg}{Ca}\right)^{t}_{sw}\right)^{H}}$$

Trace element data were also used to check the efficiency of the foraminiferal cleaning procedure[20,54]. All samples had Al/Ca ratios of <100 µmol/mol, and typically <60 µmol/mol.

Determination of pH from δ^{11}B of *G. ruber*. Boron in seawater exists mainly as two different species, boric acid ($B(OH)_3$) and borate ion ($B(OH)_4^-$), and their relative abundance is pH dependent. There are two isotopes of boron, ^{11}B (~80%) and ^{10}B (~20%), with a ratio normally expressed in delta notation as:

$$\delta^{11}\mathrm{B}(‰) = \left[\left(\frac{{}^{11}\mathrm{B}/{}^{10}\mathrm{B}_{\mathrm{sample}}}{{}^{11}\mathrm{B}/{}^{10}\mathrm{B}_{\mathrm{NIST951}}}\right) - 1\right] \mathrm{x}1000 \qquad [3]$$

where $^{11}B/^{10}B_{NIST951}$ is the isotopic ratio of NIST SRM 951 boric acid standard ($^{11}B/^{10}B = 4.04367$; ref. 60).

There is a pronounced isotopic fractionation between the two dissolved boron species, with boric acid being enriched in ^{11}B by 27.2‰ (ref. 61). As the concentration of each species is pH dependent, their isotopic composition also has to change with pH in order to maintain a constant seawater δ^{11}B. Calibration studies[54,62,63] have shown that the borate species is predominantly incorporated into foraminiferal $CaCO_3$, and therefore ocean pH can be calculated from the δ^{11}B of borate ($\delta^{11}B_{borate}$) as follows:

$$\mathrm{pH} = \mathrm{pK}^{*}_{\mathrm{B}} \quad \log \quad \frac{{}^{11}\mathrm{B}_{\mathrm{sw}} \quad {}^{11}\mathrm{B}_{\mathrm{borate}}}{{}^{11}\mathrm{B}_{\mathrm{sw}} \quad \left({}^{11\text{-}10}\mathrm{K}_{\mathrm{B}} \cdot \quad {}^{11}\mathrm{B}_{\mathrm{borate}}\right) \quad 1000\cdot\left({}^{11\ 10}\mathrm{K}_{\mathrm{B}} \quad 1\right)} \div \qquad [4]$$

where pK^{*}_{B} is the dissociation constant for boric acid at in situ temperature, salinity and pressure[64], $\delta^{11}B_{sw}$ is the isotopic composition of seawater (39.61‰; ref. 65), $\delta^{11}B_{borate}$ is the isotopic composition of borate ion, and $^{11\text{-}10}K_B$ is the isotopic fractionation between the two aqueous species of boron in seawater (1.0272±0.0006) (ref. 61).

In our calculations, temperature for ODP Site 999 is derived from Mg/Ca ratios measured on aliquots (separated after dissolution) of the same samples used for $\delta^{11}B$ analysis and for ODP Site 662 from published records of temperature using the $U^{k'}_{37}$ proxy[66]. Despite the uncertainty in Mg/Ca-derived SST's we have not used published $U^{k'}_{37}$ temperature records for ODP Site 999 because they are of lower temporal resolution and close to saturation (T = 28-29 °C)[25]. Salinity has little influence on the calculations of pH (±1 psu = ±0.006 pH units), and therefore is assumed to be constant at 35 psu (similar to the present-day mean annual average at both locations). The uncertainty associated with this assumption is propagated into pCO_2^{atm} calculations.

Boron has a long residence time in seawater (10-20 Ma; ref. 67), and to account for likely (small) changes in the boron isotopic composition of seawater ($\delta^{11}B_{sw}$) over the last 3 million years, we use a simple linear extrapolation between modern $\delta^{11}B_{sw}$ (39.61‰; ref. 65) and the $\delta^{11}B_{sw}$ determined by ref. 68 for the middle Miocene (12.72 Ma; $\delta^{11}B_{sw}$ = 37.8‰). This simple estimation yields $\delta^{11}B_{sw}$ = 39.2‰ at 3 Ma, which is consistent with available independent constraints, for example based on assumptions of bottom water pH and measured benthic foraminiferal $\delta^{11}B$ (ref. 69).

Finally, in order to calculate pH from the $\delta^{11}B$ of *G. ruber*, it is necessary to account for species-specific differences between $\delta^{11}B_{borate}$ in ambient seawater and $\delta^{11}B$ in foraminiferal calcite ($\delta^{11}B_{calcite}$; i.e., "vital effects"). Here we used the species- and size-specific calibration equation of ref. 18 for *G. ruber* 300-355 µm (Equation 5). This equation has been applied in previous studies[18] to produce a $\delta^{11}B$-based atmospheric pCO_2 (pCO_2^{atm}) record for the last 30 kyr that is in very good agreement with ice-core pCO_2^{atm} records (Extended Data Figure 2).

$$\delta^{11}B_{borate} = (\delta^{11}B_{calcite} - 8.87\pm1.52)/0.60\pm0.08 \text{ (uncertainty at } 2\sigma) \quad [5]$$

It is important to note that, not only is there generally good preservation of the sites we use[23,24], but also the $\delta^{11}B$ of *G. ruber* does not appear to be significantly affected by partial dissolution[25].

Determination of pCO_2^{atm} from $\delta^{11}B$-derived pH. Another variable of the ocean carbonate system is required besides pH in order to calculate the partial pressure of CO_2 in seawater (pCO_2^{sw})[70]. Here, total alkalinity (TA) is assumed to be constant at values similar to modern at ODP Site 999 (2330 µmol/kg; ref. 20). It is important to note that pCO_2^{sw} estimates are mostly determined by the reconstructed pH and that TA has little influence. This is because pH reflects the *ratio* of TA to DIC (total dissolved inorganic carbon), so when pH is known the ratio of TA:DIC is set, so the effect on pCO_2^{sw} of a large increase/decrease in TA is partially countered by an opposite change in DIC. Indeed, at a given pH, a change in TA by 10% only results in a pCO_2^{sw} change of 10%. For example, modifying TA by ±100 µmol/kg (a range equivalent to modelled variations in TA for the last 2 million years; ref. 30) only modifies reconstructed pCO_2^{sw} (when pH is known) by less than ±12 µatm.

pCO_2^{sw} was calculated using the equations of ref. 70, the "seacarb" package of R (ref. 71) and a Monte Carlo approach (n= 10,000) to fully propagate the uncertainty in the input parameters (at 95% confidence or full range, where appropriate): $\delta^{11}B$ (±analytical uncertainty, calculated using Equation [1], and calibration uncertainty in Equation [5]), Mg/Ca-derived temperature (±3 ^{o}C), salinity (±3 psu), TA (±175 µmol/kg), $\delta^{11}B_{sw}$ (±0.4‰). pCO_2^{atm} was then calculated from pCO_2^{sw} using Henry's Law and subtracting the modern disequilibria with respect to CO_2 at the two sites (Extended Data Figure 1; Supplementary Information Tables 1&2). Note that for the quoted uncertainty range for temperature, salinity, and $\delta^{11}B_{sw}$ a normal distribution is assumed. However, for TA we have assumed a "flat" probability (i.e. an equal probability of TA being any value between 2155 and 2505 µmol/kg). We therefore do not ascribe weight to the assumption that TA remains constant, but rather fully explore the likely range given the available, model based, constraints[72,73]. It should also be noted that salinity and temperature have little control on our estimated pCO_2^{sw} (+1 psu = +0.2 µatm; +1 ^{o}C = +8 µatm).

Comparison with published records of Pliocene pCO_2^{atm}. Figure 1 and Extended Data Figures 2b&c show a comparison of our new high resolution $\delta^{11}B$-derived pCO_2^{atm} record with published records. As noted in the main text, although the various approaches agree, in detail our new record exhibits more structure. As a consequence, cross plots of the previously published CO_2 data against ΔMAT (or SSTst) are largely incoherent (Extended Data Figure 2d-f). In the case of the stomatal estimates[50] and the existing $\delta^{11}B$-based records[23, 25] this is largely a consequence of their low temporal resolution, although analytical issues[74] and species choice (we use *G. ruber* that spends its entire life cycle in the mixed layer whereas ref. 23 uses *G. sacculifer* that migrates during its life cycle and whose $\delta^{11}B$, unlike *G.ruber*, is modified by partial dissolution[25]) may also play a role for the discrepancy with earlier $\delta^{11}B$ records (see ref. 25 for further discussion). The lack of variability through the Pliocene for the alkenone-based records may be related to changes in the size of the alkenone producers[26], fluctuations in nutrient content/water depth of maximum alkenone production, and/or variations in the degree of passive vs. active uptake of CO_2 by the alkenone producing coccolithophorids[49,75].

Continuous records of Pliocene and late Pleistocene global temperature change. Robust records of global temperature change are needed to determine how the Earth's climate has responded to changes in CO_2. Here we estimate this variable using two independent approaches: (i) we generate a stack of available sea surface temperature records (SSTst); and (ii) following ref. 35 we use a reconstruction of global mean annual surface air temperature change based on a scaling of the northern hemisphere temperature required by a simple coupled ice-sheet-climate model to forward model the benthic $\delta^{18}O$ stack of ref. 76 (tuned here to the LR04 age model; ΔMAT).

For the SST stack (SSTst) we imposed a number of criteria for site selection. These are: (i) the record must be continuous from late Pliocene to late Pleistocene (or nearly so); (ii) the temporal resolution must be relatively high (ideally better than 1 sample per 10 kyr; for ODP Site 1237 we have however accepted a lower resolution to increase spatial coverage) to allow us to fully resolve the dominant orbital-scale variability; (iii) be based on $U^{k'}_{37}$, given that Mg/Ca suffers an unacceptable level of uncertainty on these timescales due to the secular evolution of the Mg/Ca ratio of seawater (e.g., ref. 48); and (iv) the temperatures recorded by the $U^{k'}_{37}$ proxy must be less than 29 °C, above which the proxy becomes saturated and therefore unresponsive[75]. Ten published records meet these criteria (ODP Sites 982, 607, 1012, 1082, 1239, 846, 662, 722, 1237 and 1090; ref. 66, 78-85) and the locations of these sites are shown in Extended Data Figure 2b. The average temporal resolution of these records is 1 sample every ~4 kyr (ranging from ~2 to ~13 kyr) and the published age model of each site is either part of the LR04 stack or was tuned to it (see the original publications for details).

In order to stack the records, each was first converted to a relative SST record referenced to either the average of the Holocene (0-10 kyr), or mean annual modern SST if the Holocene is missing, and then linearly interpolated to a 5 kyr spacing. These relative records are then averaged to produce a single stacked record of relative SST change (SSTst; Supplementary Information Table 5). The number of sites contributing to SSTst varies but for most of the record is ≥ 8 (Extended Data Figure 6a&b). Uncertainty on SSTst is estimated by a Monte Carlo procedure where 1000 realisations are made of each individual SST record with noise added reflecting the magnitude of analytical uncertainty in the $U^{k'}_{37}$ SST reconstruction (± 1 °C at 2σ; ref. 75). Since we are using the same proxy for each location it is not necessary to consider the calibration uncertainty as this should be the same for each record. Each SST realisation is then averaged to produce 1000 realisations of SSTst. The mean of these 1000 realisations is then calculated and the 95% confidence interval is given by the 2.5% and 97.5% percentile (red band on Figure 3). Jacknifing of SSTst (i.e. the sequential removal of one record at a time) indicates that no particular record has undue influence and SSTst remains close to the bounds relating to analytical uncertainty (the grey lines on Extended Data Figure 6c&d).

Our aim with SSTst was not to specifically reconstruct global SST change but rather to examine the change in SST at these locations for a given forcing in the Pliocene and Pleistocene. We therefore do not require SSTst to reflect global SST change. However, in order to assess how well SSTst does reflect global SST we:

(i) Examined the mean of historic SST change (1870AD to 2013 AD; from the HadISST database; ref. 86) at each location where we have an alkenone palaeo-SST record. This comparison is shown in Extended Data Figure 7 (blue circles). Despite exhibiting more variability than the mean annual global average (red in Extended Data Figure 7), these 10 sites clearly capture the global long term trend in global mean SST[87,88] over the last 140 years or so (Extended Data Figure 7).

(ii) Compare SSTst to a multi-proxy and more comprehensive and independent compilation of ref. 32 that covers the last 100 kyr with >30 sites and the last 278 kyr with >10 sites. When data for the last 278 kyr are stacked together in a similar way to SSTst, the stack of ref. 32 (blue on Fig 3c) compares well with SSTst giving us confidence that it closely reflects global SST change.

(iii) Compare SSTst to discrete global reconstructions of SST. For the last glacial (20-25 kyr) SSTst gives a ΔSST of -2.2 ± 0.4 K, which is close to the ΔSST of -3.2 K from a recent comprehensive compilation for the LGM[42] and is within uncertainty of earlier reconstructions (e.g., ref. 85 where ΔSST of -1.9 ± 1.8 K). For the Mid-Pliocene Warm Period (3-3.3 Ma), SSTst gives an average of +2.3 K. A simple mean calculated from the larger multi-proxy PRISM SST compilation of ref. 40 is very similar at +2.6 K. SSTst is slightly warmer than an area weighted mean of the PRISM SST set (+2 K; ref. 40).

Taken together, these comparisons clearly indicate that, although SSTst is made of a limited number of sites, it does appear to closely reflect change in global SST. This conclusion is also supported by the general agreement between the trends (but not absolute values) exhibited by ΔMAT and SSTst through the Pliocene and Pleistocene (Fig. 3), with subtle differences between these two climate records (e.g. at 2.8 Ma) potentially a result of a decoupling between deep and surface water temperature evolution, small spatial biases in our SST stack, and/or minor age-model inaccuracies.

Regression-based determinations of climate sensitivity In order to examine the climatic response (expressed as either ΔMAT or ΔSST) to forcing by CO_2 and land-ice albedo changes in both time periods, we used a linear regression approach. Because each variable used (CO_2 and SL, ΔMAT or ΔSST) has an associated uncertainty, however, it is necessary to fully explore the influence of these uncertainties on our estimates of slope determined using least squares linear regression. Due to difficulty of performing least squares linear regression with uncertainty in X- and Y- variables that are not necessarily normally distributed we have used a two stage approach to fully propagate all the uncertainties involved. Firstly, we generated 1000 realisations of each temporal record of each variable (e.g. ΔF_{CO2}, $\Delta F_{CO2,LI}$, ΔMAT or ΔSST) based on a random sampling of each record within its uncertainty envelope. This uncertainty envelope was either a simple normal distribution (e.g. ± 6 ppm for ice-core CO_2) or based on other Monte Carlo output (e.g. random sampling the 10,000 simulations of the Pliocene $\delta^{11}B$-pCO_2^{atm} record or the 1000 realisations of SSTst; see above). Then the first realisation of the ΔF_{CO2} (or $\Delta F_{CO2,LI}$) record was regressed against the first realisation of the ΔMAT (or ΔSST) with the uncertainty in the slope and intercept of that regression determined using a bootstrapping approach (n=1000; ref. 90). The second realisation of the forcing term and the climate response was then regressed and the 1000 estimates of slope and intercept by bootstrapping were combined with 1000 of the first regression. This continued for all 1000 realisations and a probability density function for the slope and intercept, accounting for X- and Y- uncertainty, was then constructed from the combined bootstrap estimates for each realisation (n=1000000). The results of this approach are shown in Fig 5.

As noted above, pCO_2^{atm} (and hence ΔF_{CO2}) calculated from boron isotopes is a function of not only the measured $\delta^{11}B$ but also the total alkalinity (TA; or other second carbonate system variable) and, beyond the last 1 million years or so, the boron isotopic composition of seawater ($\delta^{11}B_{sw}$). This is illustrated in Extended Data Fig 8. Here pCO_2^{atm} is calculated from an artificial $\delta^{11}B$ and temperature record (Extended Data Fig 8a), a TA of either 2000 µmol/kg, 2300 µmol/kg or 2600 µmol/kg, a $\delta^{11}B_{sw}$ of 38.8, 39.6 (i.e. modern) or 40.4 ‰ (Extended Data Fig 8) and the assumption that pCO_2^{atm} = pCO_2^{sw}. These parameter choices result in a large difference in absolute CO_2 but, although they are extreme and perhaps unlikely for the Pliocene, the slope of a linear regression of global temperature change and ΔF_{CO2} is very similar for each set of parameters (Extended Data Fig 8c,d). So much so, even with only a poor knowledge of $\delta^{11}B_{sw}$ (e.g. ± 0.8 ‰) and TA (e.g. ± 300 µmol/kg) the accuracy of the relationship between reconstructed ΔF_{CO2} and temperature is not unduly impacted.

The residence time of boron in seawater (10-20 Ma) ensures that changes in $\delta^{11}B_{sw}$ across the time interval examined here (1 Myr) are unlikely to be large (<0.1 ‰; ref. 67) and so uncertainty in the absolute value of $\delta^{11}B_{sw}$ and any changes across the study interval can be ignored for our determinations of S^p. In all the previous calculations we assume that TA is randomly distributed between 2155 and 2505 µmol/kg, therefore accounting for all possible trends in TA across the time interval studied within this range. However, to better examine the influence of a large secular shift in TA on our estimates of S^p we have imposed a 200 µmol/kg decrease (TAd) or increase (TAi) across our Pliocene study interval. The slope for the regressions using one parameter set (VDW11 and sea-level from ref. 46 recalculated by ref. 12) but with such a varying TA are shown in Extended Data Fig 8e&f. Even this relatively large secular change does not have a major influence on the estimated slope, clearly illustrating that our assumptions regarding TA, both its absolute value and its secular evolution, have little influence on our calculated ΔF_{CO2} and hence our conclusions.

Pliocene pCO_2^{atm} variability The apparent cyclicity in our Pliocene CO_2 record can be investigated using spectral analysis. Extended Data Fig 4c shows the evolutive power spectra for the Pliocene pCO_2^{atm} and a ~100 kyr cycle is clearly dominant. Our sampling resolution is 1 sample ~13 kyr, which is not sufficient to resolve cycles of a precessional length (e.g. 19 and 23 kyr) but may be adequate to resolve obliquity (~41 kyr length) yet these cycles are apparently absent in the generated spectra

(Extended Data Fig 4c). To ensure our resolution is not biasing this result we have sampled the LR04 benthic δ^{18}O stack at our exact sampling resolution and examined the evolutive power spectra of this sampled record (Extended Data Fig 4d). This analysis reveals the presence of 100 kyr and 41 kyr cycles in the δ^{18}O data, despite our relatively low resolution, supporting the observation that the dominant cycle in Pliocene pCO_2^{atm} is ~100 kyr.

The magnitude of Pliocene pCO_2^{atm} variability, shown in Extended Data Fig 4a, is similar to that exhibited by published late and mid-Pleistocene δ^{11}B-pCO_2^{atm} records (green and red lines on Extended Data Fig 4a) and by the Late Pleistocene ice core data when noise that is approximately equivalent to our δ^{11}B-pCO_2^{atm} uncertainty is added (± 35 μatm; black dashed line on Extended Data Fig 4a). In contrast, the δ^{18}O variability for these time intervals increases markedly from the Pliocene to late Pleistocene as the magnitude of glacial-interglacial cycles increases (Fig 1e, Extended Data Fig 4b).

References (for Methods only)

51 Lawrence, K.T., Sigman, D.M., Herbert, T.M., Riihimaki, C.A., Bolton, C.T., Martinez-Garcia, A., Rosell-Mele, A., and Haug, G. Time-transgressive productivity changes in the North Atlantic upon Northern Hemisphere glaciation, *Paleoceanography*, 28, doi: 10.1002/2013PA002546 (2013).

52 Barker, S., Greaves, M., Elderfield, H. A study of cleaning procedures used for foraminiferal Mg/Ca paleothermometry. *Geochemistry, Geophysics, Geosystems*, 4(9): 8407, dio:10,1029/2003GC000559 (2003).

53 Yu, J., Elderfield, H., Greaves, M., Day, J. Preferential dissolution of benthic foraminiferal calcite during laboratory reductive cleaning. *Geochemistry Geophysics Geosystems*, Q06016: doi:10.1029/2006GC001571 (2007).

54 Rae, J.W.B., Foster, G.L., Schmidt, D.N., Elliott, T. Boron isotopes and B/Ca in benthic foraminifera: proxies for the deep ocean carbonate system. *Earth and Planetary Science Letters*, 302: 403-413 (2011).

55 Medina-Elizalde, M., Lea, D.W., Fantle, M.S. Implications of seawater Mg/Ca variability for Plio-Pleistocene tropical climate reconstruction. *Earth and Planetary Science Letters*, 269, 584-594 (2008).

56 Evans, D., Muller, W. Deep time foraminifera Mg/Ca paleothermometry: Nonlinear correction for secular change in seawater Mg/Ca. *Paleoceanography*, 27, PA4205, (2012).

57 Fantle, M.S., DePaolo, D.J. Sr isotopes and pore fluid chemistry in carbonate sediment of the Ontong Java Plateau: Calcite recrystallisation rates and evidence for a rapid rise in seawater Mg over the last 10 million years. *Geochim.Cosmochim. Acta* 70: 3883-3904 (2006).

58 Delaney, M. L., WH Bé, A. & Boyle, E. A. Li, Sr, Mg, and Na in foraminiferal calcite shells from laboratory culture, sediment traps, and sediment cores*. Geochim.Cosmochim. Acta* 49, 1327-1341 (1985).

59 Dekens, P.S., Lea, D.W., Pak, D.K., Spero, H.J. Core top calibration of Mg/Ca in tropical foraminifera: Refining paleotemperature estimation. *Geochemistry, Geophysics, Geosystems* (G3), 3(4): dio: 10.1029/2001GC000200 (2002).

60 Catanzaro, E.J. et al. Boric assay; isotopic, and assay standard reference materials. US National Bureau of Standards, Special Publication, 260-17, 70 pp (1970).

61 Klochko, K., Kaufman, A.J., Yoa, W., Byrne, R.H., Tossell, J.A. Experimental measurement of boron isotope fractionation in seawater. *Earth and Planetary Science Letters*, 248: 261-270 (2006).

62 Hemming, N.G., Hanson, G.N. Boron isotopic composition and concentration in modern marine carbonates. *Geochimica et Cosmochimica Acta*, 56: 537-543 (1992).

63 Hemming, N.G., Reeder, R.J., Hanson, G.N., 1995. Mineral-fluid partitioning and isotopic fractionation of boron in synthetic calcium carbonate. *Geochimica et Cosmochimica Acta*, 59(2): 371-379 (1995).

64 Dickson, A. G. Thermodynamics of the dissociation of boric-acid in synthetic seawater from 273.15 to 318.15 K. *Deep-Sea Res.* **37**, 755-766 (1990).

65 Foster, G.L., Pogge von Strandmann, P.A.E., Rae, J.W.B. Boron and magnesium isotopic composition of seawater. *Geochemistry Geophysics Geosystems*, 11(8): Q08015, doi:10.1029/2010GC003201 (2010).

66 Herbert, T.D., Cleaveland Peterson, L., Lawrence, K.T., Liu, Z.Tropical Ocean Temperatures Over the Past 3.5 Million Years. *Science*, 328: 1530-1534 (2010).

67 Lemarchand, D., Gaillardet, J., Lewin, E., Allegre, C.J. Boron isotope systematics in large rivers: implications for the marine boron budget and paleo-pH reconstruction over the Cenozoic. *Chemical Geology*, 190: 123-140 (2002).

68 Foster, G.L., Lear, C.H., Rae, J.W.B. The evolution of pCO_2, ice volume and climate during the middle Miocene. *Earth and Planetary Science Letters*, 341-344: 243-254 (2012).

69 Raitzsch, Hönisch, B. Cenozoic boron isotope variations in benthic foraminifers. *Geology*, 41(5): 591-594 (2013).

70 Zeebe, R., Wolf-Gladrow, D.A. CO_2 in Seawater: Equilibrium, Kinectics, Isotopes. Elsevier Oceanography Series 65. Elsevier, Amesterdam, 346 pp (2001).

71 R Core Team, R: A language and environment for statistical computing. R Foundation for Statistical Computing, Vienna, Austria. ISBN 3-900051-07-0, URL http://www.R-project.org/ (2013).

72 Tyrrell, T., Zeebe, R.E. History of carbonate ion concentration over the last 100 million years. *Geochimica et Cosmochimica Acta*, 68(17): 3521-3530 (2004).

73 Clark, P.U. et al. The middle Pleistocene transition: characteristics, mechanisms, and implications for long-term changes in pCO_2. *Quarternary Science Reviews*, 25: 3150-3184 (2006).

74 Foster, G. L. et al. Interlaboratory comparison of boron isotope analyses of boric acid, seawater and marine $CaCO_3$ by MC-ICPMS and NTIMS. *Chemical Geology* 358, 1-14, doi:http://dx.doi.org/10.1016/j.chemgeo.2013.08.027 (2013).

75 Bolton, C. T., Stoll, H. M., Mendez-Vicente, A. Vital effects in coccolith calcite: Cenozoic climate-pCO_2 drove the diversity of carbon acquisition strategies in coccolithophores? *Paleoceanography* 27 (2012).

76 Zachos, J., Pagani, M., Sloan, L., Thomas, E., Billups, K. Trends, rythms, and aberrations in global climate 65 Ma to present. *Science*, 292: 686-693 (2001).

77 Müller, P. J., Kirst, G., Ruhland, G., Von Storch, I. & Rosell-Melé, A. Calibration of the alkenone paleotemperature index UK'37 based on core-tops from the eastern South Atlantic and the global ocean (60 N-60 S). *Geochim. Cosmochim. Acta* 62, 1757-1772 (1998).

78 Lawrence, K.T., Herbert, T.D., Brown, C.M., Raymo, M.E., Haywood, A.M. High-amplitude variations in North Atlantic sea surface temperature during the early Pliocene warm period. *Paleoceanography*, 24(PA2218): doi: 10.1029/2008PA001669 (2009).

79 Lawrence, K.T., Sosdian, S., White, J.M., Rosenthal, Y. North Atlantic climate evolution through the Plio-Pleistocene climate transistions. *Earth and Planetary Science Letters*, 300: 329-342 (2010).

80 Brierley, C.M. et al. Greatly expanded tropical warm pool and weakened Hadley Circulation in the Early Pliocene. *Science*, 323: 1714-1718 (2009).

81 Etourneau, J., Martinez, P., Blanz, T., Schneider, R. Pliocene-Pleistocene variability of upwelling activity, productivity, and nutrient cycling in the Benguela Region. *Geology*, 37(10): 871-874 (2009).

82 Etourneau, J., Schneider, R., Blanz, T., Martinez, P. Intensification of the Walker and Hadley atmospheric circulations during the Pliocene-Pleistocene climate transition. *Earth and Planetary Science Letters*, 297: 103-110 (2010).

83 Lawrence, K.T., Liu, Z., Herbert, T.D. Evolution of the Eastern Tropical Pacific Through Plio-Pleistocene Glaciation. *Science*, 312: 79-83 (2006).

84 Martinez-Garcia, A., Rosell-Melé, A., McClymont, E.L., Gersonde, R., Haug, G.H. Subpolar link to the emergence of the modern equatorial Pacific cold tongue. *Science*, 328: 1550-1553 (2010).

85 Dekens, P. S., Ravelo, A. C. & McCarthy, M. D. Warm upwelling regions in the Pliocene warm period. *Paleoceanography* 22 (2007).

86 Rayner, N. A. et al. Global analyses of sea surface temperature, sea ice, and night marine air temperature since the late nineteenth century. *Journal of Geophysical Research: Atmospheres* 108, 4407, doi:10.1029/2002jd002670 (2003).

87 Kennedy, J.J., Rayner, N.A., Smith, R.O., Parker, D.E., Saunby, M. Reassessing biases and other uncertainties in sea surface temperature observations in situ since 1850: 1. Measurement and sampling uncertainty. *Journal of Geophysical Research*, 116, D14103: doi:10.1029/2010JD015218 (2011a).

88 Kennedy, J.J., Rayner, N.A., Smith, R.O., Parker, D.E., Saunby, M. Reassessing biases and other uncertainties in sea surface temperature observations measured in situ since 1850: 2. Biases and homogenization. *Journal of Geophysical Research*, 116, D14104, (2011b).

89 Waelbroeck, C. et al., Constraints on the magnitude and patterns of ocean cooling at the Last Glacial Maximum. *Nature Geoscience*, 2: 127-132, (2009).

90 Efron, B. Bootstrap Methods: another look at the Jacknife. Annals of Statistics, 7: 1-26 (1979).

91 Locarnini, R. A. et al. World Ocean Atlas 2013, Volume 1: Temperature. NOAA Atlas NESDIS 73, 40 pp (2013).

92 Schlitzer, R., Ocean Data View, http://odv.awi.de (2012).

93 Siddall, M. et al. Sea-level fluctuations during the last glacial cycle. *Nature*, 423: 853-858 (2003).

Figure Legends for Extended Data Figures

Extended Data Figure 1. Maps of modern mean annual ΔpCO_2 and sea surface temperature labelled with site locations. (a) Map of sites used for pCO_2^{atm} reconstruction with the mean annual modern ΔpCO_2 from the reconstruction of ref. 21. (b) Map of the sites (and labelled with their depths) used to generate SSTst with mean annual modern SST from the World Ocean Atlas 2013 (ref. 91). Figures constructed and data visualised in Ocean Data View[92].

Extended Data Figure 2. Comparisons of boron isotope based-pCO_2^{atm} estimates with other methodologies and archives. (a) Estimates of pCO_2^{atm} from published $\delta^{11}B$-records compared to ice-core CO_2 (red line; ref. 27-29). The dotted line is for $pCO_2 = 278$ μatm. In (a) the data of ref. 20 (blue circles) have been recalculated in the same manner as described here for the Pliocene, including using the *G. ruber* $\delta^{11}B$-pH calibration of ref. 18. Error band encompasses 68% (dark blue) and 95% (light blue) of 10,000 Monte Carlo simulations of pCO_2^{atm} (as described in text). Also shown are the *G. sacculifer* based $\delta^{11}B$-pCO_2^{atm} record of ref. 30 (green circles). In this case error bars (± 25 μatm) are as determined in that study. Despite similar analytical uncertainty, the smaller error bars for the ref. 30 data result from these authors not propagating the $\delta^{11}B$-pH calibration uncertainty and considering a smaller range in temperature, salinity and alkalinity uncertainty than in this study (± 0.76 °C, ± 1 psu, ± 27 μmol/kg vs. ±3 °C, ± 3 psu, ± 175 μmol/kg with a flat probability in this study). (b) $\delta^{11}B$-based pCO_2^{atm} record generated here (blue closed circles and 95% and 68% uncertainty band) with pCO_2^{atm} from the $\delta^{13}C$ of alkenones from published studies. See caption for Figure 1 for details. (c) $\delta^{11}B$-based pCO_2^{atm} record generated here (blue closed circles and 95% and 68% uncertainty band) with pCO_2^{atm} from previous $\delta^{11}B$-based studies and from plant stomata. See caption for Figure 1 for details. (d – f) Comparison of cross plots of CO_2 forcing and ΔMAT for our high resolution $\delta^{11}B$-CO_2 record (d), published alkenone-CO_2 (e) and published low resolution $\delta^{11}B$-CO_2 (f). In each panel the slopes of regression lines fitted through the data are labelled (± 1 se). In (d) ice-core CO_2 are shown in red open circles and Pliocene $\delta^{11}B$-CO_2 in open blue circles. In (e) and

(f) ice-core CO_2 data are shown in grey for clarity. In (e) alkenone-CO_2 data are from the following sources: ODP 1208 (orange, ref. 16), ODP 806 (purple, ref. 16); ODP 925 (brown, ref. 49); ODP 999 (green circles = ref. 25; green squares = ref. 26). In (c) δ^{11}B-CO_2 are from ODP999 (blue[25] and red[23]).

Extended Data Figure 3. Probability density functions for equivalent aged samples from ODP Site 662 and ODP Site 999. Each panel, labelled with age in ka, shows the probability density function for a given estimate of pCO_2^{atm} from ODP Site 662 (red) and ODP Site 999 (blue). In most instances equal age samples are compared, but in some cases either where variability is high and/or equivalent age samples are absent, we show neighbouring samples from ODP Site 999 (e.g. bottom left and right). This comparison indicates that although the mean pCO_2^{atm} of ODP 662 tends to be higher than ODP 999, there is always significant overlap between the estimates from the two sites.

Extended Data Figure 4. Probability density functions of pCO_2^{atm} and benthic δ^{18}O and time series analysis. (a) Probability density functions (pdf) of the residuals of δ^{11}B-pCO_2^{atm} about the long-term trend for the late Pliocene (this study; blue line), the mid-Pleistocene[30] (green line) and late-Pleistocene[19,20,21] (red line). Dashed vertical lines show the upper and lower limit (labelled in figure) encompassing 90 % of the data. The residual of the ice-core CO_2 record[27-29] about the long-term mean for 0 – 0.8 Ma plus a random noise equivalent to ± 35 μatm (the typical δ^{11}B-CO_2 uncertainty) is shown as a black dashed pdf. (b) Probability density functions of the residual of LR04 benthic δ^{18}O from the long-term trend for the late-Pleistocene (red), mid-Pleistocene (green) and late Pliocene (blue). Dashed vertical lines show the upper and lower limit (labelled in figure) encompassing 90% of the data. In contrast to the pCO_2^{atm}, δ^{18}O clearly exhibits an increase in variability over the last 3.3 million years. (c) Evolutive power spectral analyses of Pliocene pCO_2^{atm} and resampled δ^{18}O (d). The evolutive power spectra was computed using the fast Fourier transform of overlapping segments with a 300,000-year moving window. Before spectral analysis, all series were notch-filtered to remove the long-term trend (bandwith = 0.005), and interpolated to 12 kyr intervals (the real resolution of our record is ~13.5 kyr).

Extended Data Figure 5. Summary of sea-level records used to calculate ΔF_{LI}. In (a) and (b) the red curve is from ref. 13 (R14) based on the planktic δ^{18}O from the Mediterranean Sea and the methods developed for the Red Sea by ref. 89. We have removed those intervals identified as possible Sapropel events and linearly interpolated across gaps in the original record. The black curve is the sea-level record from an inversion of the benthic oxygen isotope record of ref. 72 (tuned to LR04 here) using an ice sheet model[35] (VDW11). The blue curve in (a) is based on the planktic/bulk δ^{18}O from the Red Sea[44] for the interval 0-520 ka and the paired Mg/Ca and benthic δ^{18}O from the deep South Pacific for the interval 520-800 ka[45] (R09+E12). The green curve in (b) is based on a scaling of the LR04 δ^{18}O stack to indicators of sea-level from sequence stratigraphy (ref. 46 recalculated by ref. 12). In each the uncertainty in the reconstruction at 95% confidence is shown by an appropriately coloured error band. Marine isotope stages mentioned in text are labelled.

Extended Data Figure 6. Stacked sea surface temperature record (SSTst). (a) and (b) Number of records that contribute to SSTst through time. (c) and (d) uncertainty in SSTst due to analytical uncertainty (at 95% confidence; red band) and showing the influence of jacknifing (i.e. removing one record at a time; grey lines show maximum and minimum). Note that the jacknifing illustrates that no one record has undue influence on SSTst.

Extended Data Figure 7. Comparison of global SST from HadSST3 dataset with SST HadISST1 from ODP sites. (a) Historic global mean annual sea surface temperature anomaly from the HadSST3 dataset[87-88] (red circles) and mean SST at locations above the ODP sites that make up SSTst from HadISST1 (blue; local SST). Thick red and blue lines are non-parametric smoothers through both datasets. (b) Cross plot of global mean annual SST and local SST. The regression line determined using linear regression has a slope of ~1 and intercept of close to 0, therefore, local SST captures the global trend well. The shaded blue band in (b) represents the 95% confidence interval of the regression line.

Extended Data Figure 8. The influence of TA and $\delta^{11}B_{sw}$ on determinations of S^p using linear regression. Artificial $\delta^{11}B$ record (a) and temperature record (b). Cross plot and regressions of $\delta^{11}B$-ΔF_{CO2} and global temperature for dramatically varying total alkalinity from 2000 to 2600 µmol/kg (TA; c) and $\delta^{11}B_{sw}$ from 38.8 to 40.4 ‰ (d). The slopes of the regressions, which are very similar regardless of parameter choice, are colour coded and listed in the bottom right hand corner of (c) and (d). (e) Probability density function of slope for regressions of Pliocene-aged ΔMAT against ΔF_{CO2} and (f) $\Delta F_{CO2,LI}$, where TA is decreasing by 200 (dashed) and increasing by 200 µmol/kg (dotted). Note that despite large variations in TA the slope of the regressions do not change significantly.

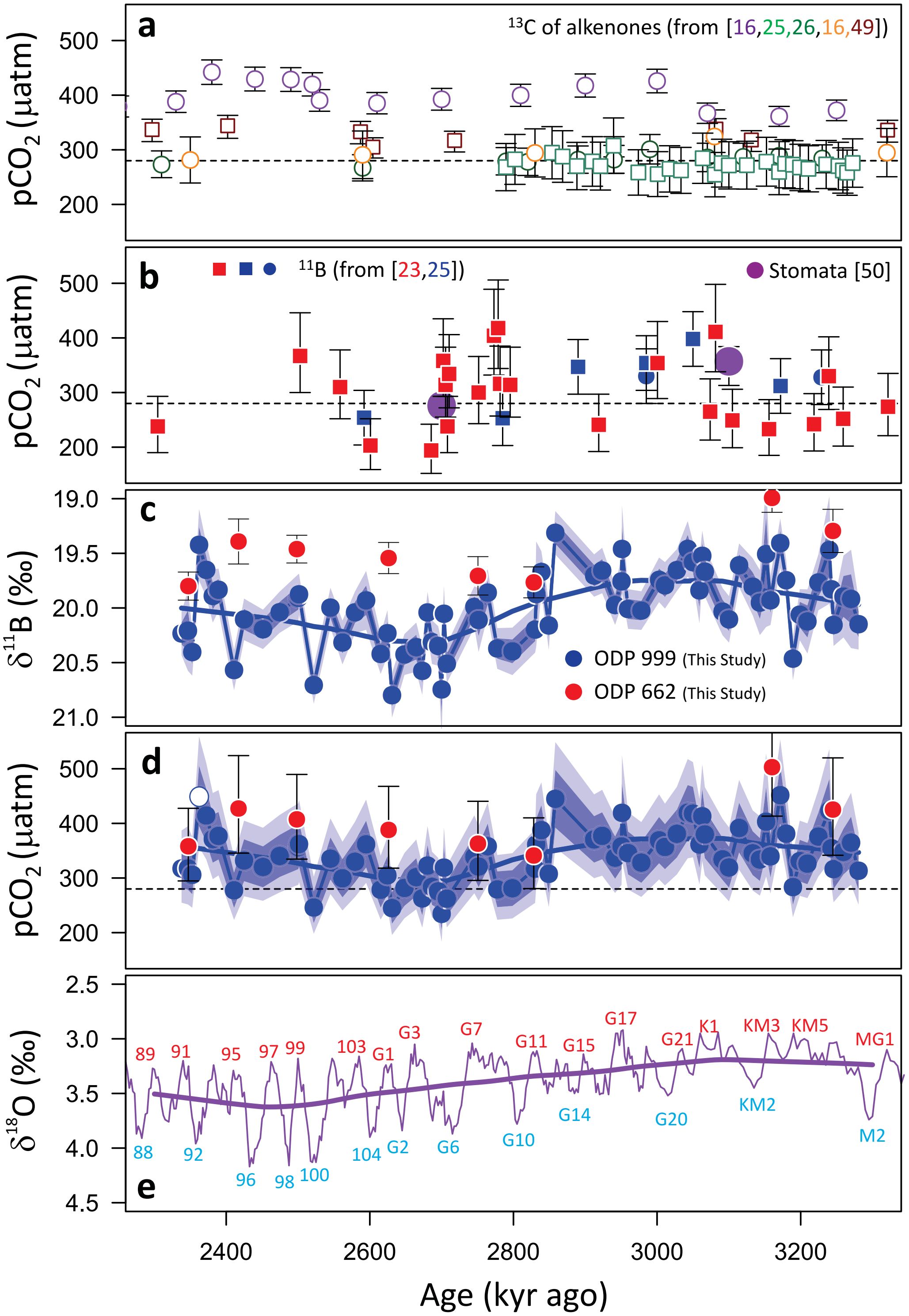
a
¹³C of alkenones (from [16,25,26,16,49])
pCO₂ (µatm)
500
400
300
200
b
¹¹B (from [23,25])
Stomata [50]
pCO₂ (µatm)
500
400
300
200
c
δ¹¹B (‰)
19.0
19.5
20.0
20.5
21.0
ODP 999 (This Study)
ODP 662 (This Study)
d
pCO₂ (µatm)
500
400
300
200
e
δ¹⁸O (‰)
2.5
3.0
3.5
4.0
4.5
89
91
95
97
99
103
G1
G3
G7
G11
G15
G17
G21
K1
KM3
KM5
MG1
88
92
96
98
100
104
G2
G6
G10
G14
G20
KM2
M2
2400
2600
2800
3000
3200
Age (kyr ago)

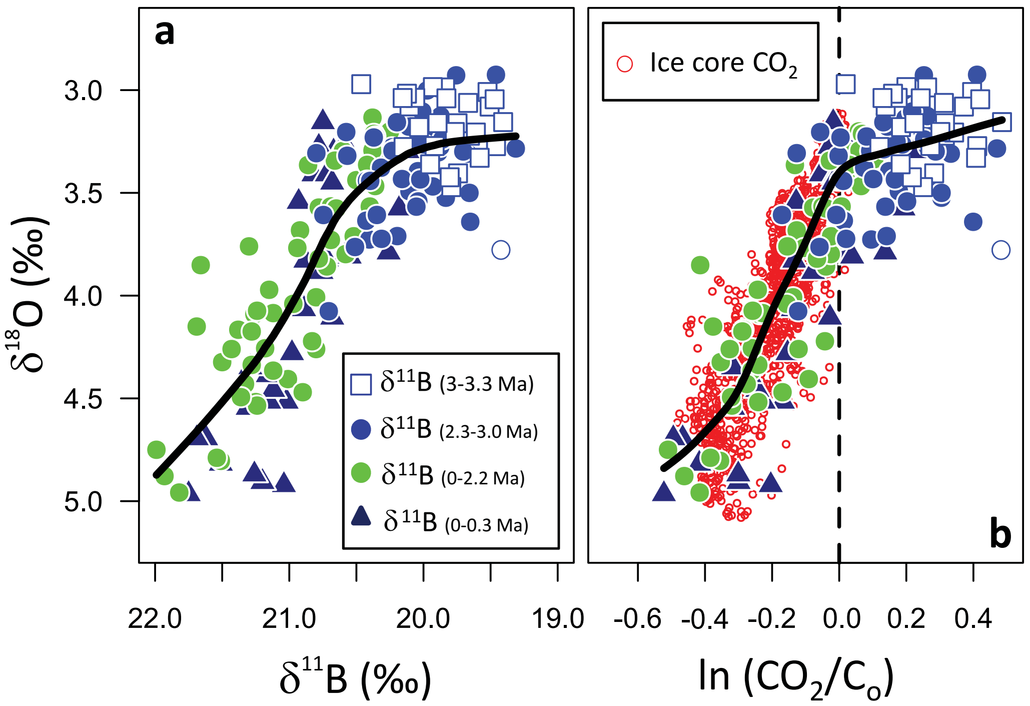
a
3.0
3.5
4.0
4.5
5.0
δ^{18}O (‰)
δ^{11}B (3-3.3 Ma)
δ^{11}B (2.3-3.0 Ma)
δ^{11}B (0-2.2 Ma)
δ^{11}B (0-0.3 Ma)
22.0
21.0
20.0
19.0
δ^{11}B (‰)
Ice core CO_2
b
-0.6
-0.4
-0.2
0.0
0.2
0.4
ln (CO_2/C_o)

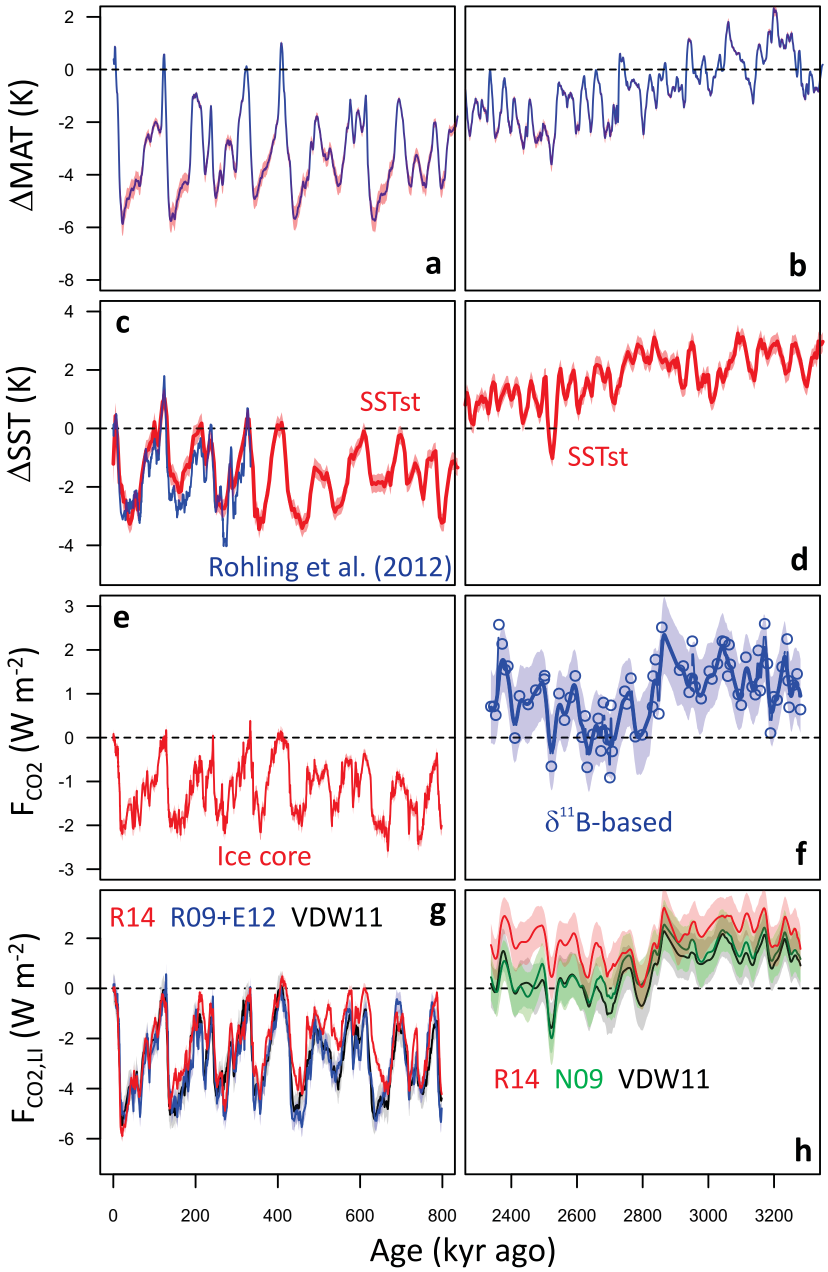ΔMAT (K)
ΔSST (K)
F_{CO2} (W m^{-2})
$F_{CO2,LI}$ (W m^{-2})
a
b
c
d
e
f
g
h
SSTst
SSTst
Rohling et al. (2012)
Ice core
δ^{11}B-based
R14 R09+E12 VDW11
R14 N09 VDW11
Age (kyr ago)
0
200
400
600
800
2400
2600
2800
3000
3200
2
0
-2
-4
-6
-8
4
3
1
-1
-3

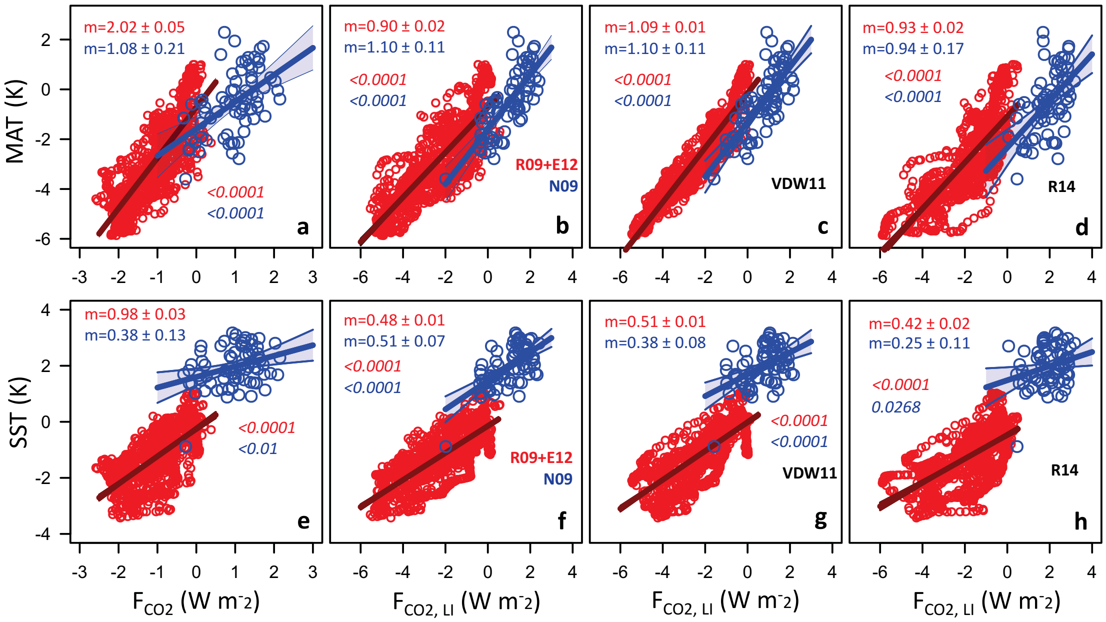
MAT (K)
SST (K)
m=2.02 ± 0.05
m=1.08 ± 0.21
<0.0001
<0.0001
a
m=0.90 ± 0.02
m=1.10 ± 0.11
<0.0001
<0.0001
R09+E12
N09
b
m=1.09 ± 0.01
m=1.10 ± 0.11
<0.0001
<0.0001
VDW11
c
m=0.93 ± 0.02
m=0.94 ± 0.17
<0.0001
<0.0001
R14
d
m=0.98 ± 0.03
m=0.38 ± 0.13
<0.0001
<0.01
e
m=0.48 ± 0.01
m=0.51 ± 0.07
<0.0001
<0.0001
R09+E12
N09
f
m=0.51 ± 0.01
m=0.38 ± 0.08
<0.0001
<0.0001
VDW11
g
m=0.42 ± 0.02
m=0.25 ± 0.11
<0.0001
0.0268
R14
h
2
0
-2
-4
-6
4
2
0
-2
-4
-3 -2 -1 0 1 2 3
-6 -4 -2 0 2 4
F_{CO2} (W m^{-2})
$F_{CO2,\ LI}$ (W m^{-2})
$F_{CO2,\ LI}$ (W m^{-2})
$F_{CO2,\ LI}$ (W m^{-2})

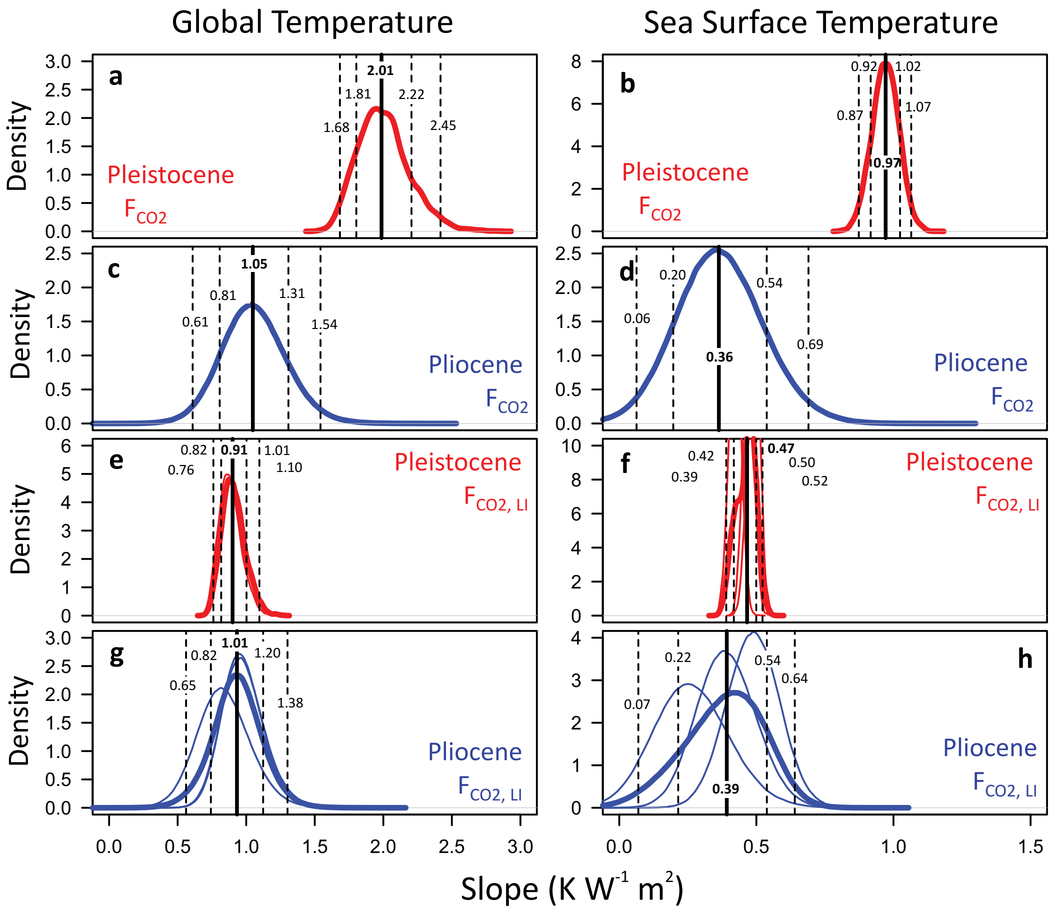
Global Temperature
Sea Surface Temperature
a
Pleistocene
F_{CO2}
1.68
1.81
2.01
2.22
2.45
b
Pleistocene
F_{CO2}
0.87
0.92
0.97
1.02
1.07
c
Pliocene
F_{CO2}
0.61
0.81
1.05
1.31
1.54
d
Pliocene
F_{CO2}
0.06
0.20
0.36
0.54
0.69
e
Pleistocene
$F_{CO2, LI}$
0.76
0.82
0.91
1.01
1.10
f
Pleistocene
$F_{CO2, LI}$
0.39
0.42
0.47
0.50
0.52
g
Pliocene
$F_{CO2, LI}$
0.65
0.82
1.01
1.20
1.38
h
Pliocene
$F_{CO2, LI}$
0.07
0.22
0.39
0.54
0.64
Density
Slope (K W^{-1} m^{2})
0.0
0.5
1.0
1.5
2.0
2.5
3.0